AAS 15-344

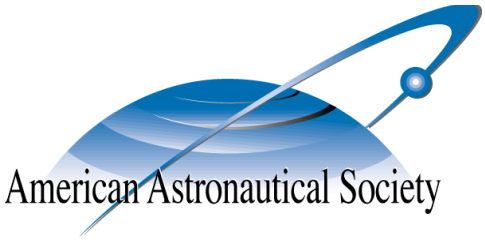

American Institute of
Aeronautics and Astronautics

GYRO ACCURACY AND FAILURE SENSITIVITY OF UNDERDETERMINED COARSE SUN-DIRECTION ESTIMATION

Stephen A. O'Keefe and Hanspeter Schaub

AAS/AIAA Spaceflight Mechanics Meeting

Williamsburg, Virginia **January 11–15, 2015**

AAS Publications Office, P.O. Box 28130, San Diego, CA 92198

AAS 15-344

GYRO ACCURACY AND FAILURE SENSITIVITY OF UNDERDETERMINED COARSE SUN-DIRECTION ESTIMATION

Stephen A. O'Keefe* **and Hanspeter Schaub†**

Coarse sun sensors are commonly used to perform coarse attitude estimation and point a spacecraft's solar arrays at the Sun. These sensors are attractive due to their relative inexpensiveness, small size, and minimal power consumption. While, traditionally, these sensors are used in large quantities to ensure redundant sensor coverage over the entire attitude sphere, this research examines underdetermined configurations where not enough sensors are available to uniquely determine the sun-direction vector at any one time. The sensitivities of two coarse sun sensor based sun-direction estimation techniques, using underdetermined sensor configurations, to rate gyroscope noise and sensor failure are presented. The relative performance of these schemes when using the spectrum of rate accuracy between inertial grade and MEMS gyroscopes is examined. In addition, the sensitivity of these methods to sensor failure is examined along with a method of improving estimation accuracy when sensor failure occurs.

INTRODUCTION

Cosine-type Coarse Sun Sensors (CSS) output a voltage relative to the input solar irradiance and are attractive sensors for small satellites due to their inexpensiveness, small size, and minimal power consumption. These sensors are often used, in concert with other sensors,[1,2] during launch deployment to accurately point a spacecraft's solar arrays at the Sun to achieve power positiveness or to perform coarse attitude determination. The size and cost requirements of increasingly popular small satellites are a driving factor for making the most of small inexpensive sensors. There is significant research into improving sun sensors; high accuracy sun sensors combine multiple measurements[3] or use Charge-Couple-Devices (CCDs)[4] to determine the direction of the Sun, but investigations into maximizing the performance of existing sensors are valuable and needed.

The performance of two different methods for CSS sun-direction estimation are examined for various levels of rate gyroscope accuracy, ranging from high-performance inertial units to inexpensive MEMS gyroscopes, and in the face of sensor failure. The first scheme is a deterministic single-point estimator that uses a combination of weighted least squares and minimum norm estimation. The second scheme is based on a hybrid continuous-discrete extended Kalman filter. Both methods use a state vector composed of a scaled sun-direction vector that is insensitive to common sensor calibration errors and neither requires knowledge of the spacecraft's inertial position in order to estimate a sun-direction vector. It has been previously shown[5] that these two methods, used in conjunction with a control algorithm, are capable of quickly and accurately pointing a spacecraft's solar arrays at the Sun despite significant state and measurement biases and noise. Reference 5 also

*Graduate Research Assistant, Aerospace Engineering Sciences, University of Colorado, Boulder, CO
†Professor, Aerospace Engineering Sciences, University of Colorado, Boulder, CO, AAS Fellow

shows how both the Weighted Least Squares Minimum Norm (WLSMN) and Extended Kalman Filter (EKF) methods are capable of performing simultaneous sun-direction estimation and control even if there is no rate measurements available. However, performance is significantly reduced. It is desirable to be able to ascertain the level of gyroscope needed in order to achieve power-positive mission attitude requirements.

This paper examines the sensitivity of these schemes to rate gyroscope noise to determine the necessary sensor accuracy to provide robust system performance. In addition, while there is literature describing the best approaches for placing sensors to guarantee redundant sensor coverage over the entire attitude sphere,[6,7] this paper examines the performance of partially underdetermined* sensor configurations suffering from known sensor failure. Such a configuration is a possibility for both inexpensive small satellites and larger satellites looking to extend mission life as components fail.

An overview of the CSS model is presented with details about the Earth albedo model used. Next the two estimation techniques used are reviewed. Numerical simulation results are presented showing the performance of the EKF based method for varying levels of rate gyro accuracy and these are compared to the weighted least squares method results. Finally, the performance of both methods in the face of a known single CSS sensor failure is shown.

COARSE SUN SENSORS

The output voltage of a CSS can be modeled, assuming Lambert's cosine law,[8] as

$$V = C\left(\boldsymbol{n}^T \frac{\boldsymbol{s}}{\|\boldsymbol{s}\|} - \frac{F_\alpha}{F_\odot} + \nu_V\right) \tag{1}$$

where $\boldsymbol{n}$ is the unit surface normal of the CSS, $\boldsymbol{s}$ is the sun-direction vector in the body frame, C is a calibration factor, and ν_v is a zero-mean Gaussian random variable included to compensate for sensor noise and model errors. The flux seen by the CSS due to the diffuse reflectance of the Earth is modeled as[1,9]

$$F_\alpha = -\frac{F_\odot}{\pi} \iint_{\boldsymbol{A}} \frac{\alpha}{\|\boldsymbol{r}_{AB}\|^2} \left(\boldsymbol{n}_A^T \frac{\boldsymbol{s}_\oplus}{\|\boldsymbol{s}_\oplus\|}\right) \left(\boldsymbol{n}_A^T \frac{\boldsymbol{r}_{AB}}{\|\boldsymbol{r}_{AB}\|}\right) \left(\boldsymbol{n}^T \frac{\boldsymbol{r}_{AB}}{\|\boldsymbol{r}_{AB}\|}\right) \mathrm{d}A \tag{2}$$

where $F_\odot$ is the solar irradiance in the vicinity of the Earth; $\boldsymbol{A}$ is the surface of the Earth visible to the spacecraft that is also illuminated by the Sun; $\boldsymbol{n}_A$ is the unit normal of a differential area of $\boldsymbol{A}$; $\boldsymbol{s}_\oplus$ is the direction vector from the Earth to the Sun; $\boldsymbol{r}_{AB}$ is a vector from $\mathrm{d}A$ to the body of the spacecraft; and α is the albedo, or reflectivity coefficient, of $\mathrm{d}A$.

The value of the Earth's albedo coefficient is highly dependent on latitude and longitude, weather patterns, and seasonal changes. Five years of daily measurements, over a $5^\circ \times 5^\circ$ latitude longitude grid, are used to calculate mean and standard deviation values that are used in numerical simulations to create statistically accurate albedo values. The albedo data used in this study were acquired as part of the NASA's Earth-Sun System Division and archived and distributed by the Goddard Earth Sciences (GES) Data and Information Services Center (DISC) Distributed Active Archive Center (DAAC).

*In the absence of noise, the sun direction can be uniquely determined at a given time if the Sun is observed by three or more CSS. An underdetermined configuration is one in which three sensor coverage is not available over the entire attitude sphere.

It is assumed the true unit direction vector for a CSS can be spherically expressed in the spacecraft body frame as

$$^{\mathcal{B}}\boldsymbol{n} = \begin{bmatrix} \cos\Big(\phi + \phi_\beta\Big)\cos\Big(\theta + \theta_\beta\Big) & \cos\Big(\phi + \phi_\beta\Big)\sin\Big(\theta + \theta_\beta\Big) & \sin\Big(\phi + \phi_\beta\Big) \end{bmatrix}^T \tag{3}$$

where θ is the azimuth angle, measured positive from the body $+x$-axis around the $+z$-axis, and ϕ is the elevation angle, measured positive toward the body $+z$-axis from the x-y plane, of the CSS unit direction vector; and θ_β and ϕ_β are uncorrelated random constants

$$\mathrm{E}\big[\theta_\beta\big] = 0, \quad \mathrm{E}\big[\theta_\beta^2\big] = \sigma_{\theta_\beta}^2, \quad \mathrm{E}\big[\phi_\beta\big] = 0, \quad \mathrm{E}\big[\phi_\beta^2\big] = \sigma_{\phi_\beta}^2, \quad \mathrm{E}\big[\phi_\beta\theta_\beta\big] = 0 \tag{4}$$

corresponding to misalignment errors. Assuming ψ is the half angle of the CSS field of view, Equation (1) becomes

$$\begin{gathered} V = C \cdot C_\kappa \left(V_d + V_\alpha + \nu_V\right) \\ V_d = \begin{cases} \boldsymbol{n}^T \frac{\boldsymbol{s}}{\|\boldsymbol{s}\|} & \text{if } \boldsymbol{n}^T \frac{\boldsymbol{s}}{\|\boldsymbol{s}\|} \geq \cos\psi \\ 0 & \text{if } \boldsymbol{n}^T \frac{\boldsymbol{s}}{\|\boldsymbol{s}\|} < \cos\psi \end{cases} \\ V_\alpha = \begin{cases} -\frac{1}{\pi} \iint\limits_{\boldsymbol{A}} \dfrac{\alpha}{\left\|\boldsymbol{r}_{AB}\right\|^2} \left(\boldsymbol{n}_A^T \dfrac{\boldsymbol{s}_\oplus}{\left\|\boldsymbol{s}_\oplus\right\|}\right) \left(\boldsymbol{n}_A^T \dfrac{\boldsymbol{r}_{AB}}{\left\|\boldsymbol{r}_{AB}\right\|}\right) \left(\boldsymbol{n}^T \dfrac{\boldsymbol{r}_{AB}}{\left\|\boldsymbol{r}_{AB}\right\|}\right) \mathrm{d}A & \text{if } B \notin \boldsymbol{\mathcal{S}} \\ 0 & \text{if } B \in \boldsymbol{\mathcal{S}} \end{cases} \end{gathered} \tag{5}$$

where B is the spacecraft's position in orbit, $\boldsymbol{\mathcal{S}}$ is the region of the spacecraft's orbit in the shadow of the Earth, and C_κ is a constant random scale factor

$$\mathrm{E}[C_\kappa] = 1, \quad \mathrm{E}\big[C_\kappa^2\big] = \sigma_{C_\kappa}^2 \tag{6}$$

included to account for error in the knowledge of the calibration coefficient. Over time, radiation and other factors may cause the parameter C_κ to change, but it is assumed to be constant over short time scales.

The spacecraft used for this study is assumed to be equipped with eight cosine-type CSS in a dual pyramid configuration. Eight sensors with 120° edge-to-edge fields of view are arranged on the $+z$ and $-z$ faces of the spacecraft oriented 90° apart and angled 45° from the body z axis. The $-z$ facing sensors are rotated by 45° about the z axis with respect to the $+z$ facing sensors. An illustration of this configuration and the associated sensor map, shown using a Lambert cylindrical area preserving projection,[10] are shown in Figure 1.

SUN-DIRECTION ESTIMATION

It is important to note that accounting for the effects of Earth albedo in the measurement model of the CSS requires both an inertial reference sun-direction vector and a spacecraft position estimate. It is assumed here as a worst-case scenario that this information is not available; a situation that might occur immediately after launch vehicle separation before ground communication has been established. Without the ability to model the Earth's albedo its impact on CSS measurements is

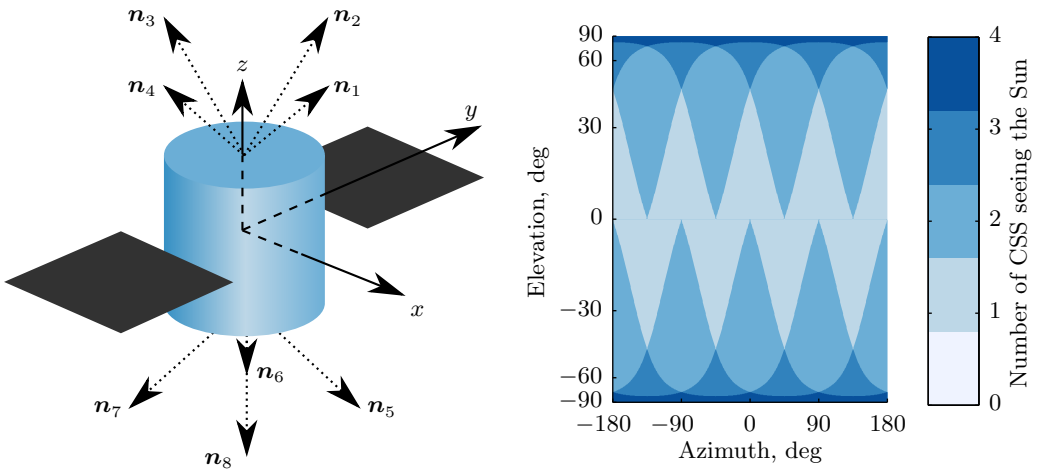

(a) Schematic of spacecraft.

(b) CSS coverage map.

Figure 1: Illustration of spacecraft, with CSS unit vectors, for an offset dual pyramid configuration and the associated coverage map.

treated as a systematic bias V_{α_β} and Equation (5) is modified to

$$V = C \cdot C_\kappa \left(V_d + V_{\alpha_\beta} + \nu_V \right)$$
$$V_d = \begin{cases} \boldsymbol{n}^T \frac{\boldsymbol{s}}{\|\boldsymbol{s}\|} & \text{if } \boldsymbol{n}^T \frac{\boldsymbol{s}}{\|\boldsymbol{s}\|} \geq \cos\psi \\ 0 & \text{if } \boldsymbol{n}^T \frac{\boldsymbol{s}}{\|\boldsymbol{s}\|} < \cos\psi \end{cases}. \tag{7}$$

Despite this significant assumption, the estimation algorithms developed here are shown to perform coarse sun-direction estimation adequate for satellite health monitoring and safe-mode maneuvering to power-positive orientations.

WEIGHTED LEAST SQUARES MINIMUM NORM (WLSMN) METHOD

Assuming the irradiance recieved due to albedo is small*, and that the common calibration factor C is not known, Equation (7) can be written in terms of a scaled sun-direction vector $\boldsymbol{d} \equiv C\boldsymbol{s}$ as

$$\begin{bmatrix} V_1 \\ \vdots \\ V_N \end{bmatrix} = \begin{bmatrix} \hat{C}_{\kappa_1} \hat{\boldsymbol{n}}_1 \\ \vdots \\ \hat{C}_{\kappa_N} \hat{\boldsymbol{n}}_N \end{bmatrix} \boldsymbol{d} + \begin{bmatrix} \nu_1 \\ \vdots \\ \nu_N \end{bmatrix} \tag{8}$$

If some estimate of the individual biases are available, from ground or on-orbit calibration, they can be substituted instead of the nominal values of $\hat{C}_{\kappa_i} = 1.0$, $\hat{\theta}_\beta = 0.0$, and $\hat{\phi}_\beta = 0.0$. Noting this measurement model is of the same form as the tradition least squares problem, if there are at least three measurements, the best estimate of the state is given by the least squares solution[11]

$$\hat{\boldsymbol{x}} = \left(\boldsymbol{H}^T \boldsymbol{W} \boldsymbol{H} \right)^{-1} \boldsymbol{H}^T \boldsymbol{W} \tilde{\boldsymbol{y}} \tag{9}$$

*Assuming the bias due to albedo is small is a significant assumption, however, this leads to a linear form and numerical Monte Carlo results show that the resulting coarse pointing performance, when coupled with a control algorithm, is sufficient for coarse sun pointing.

where $\boldsymbol{W}$ is a diagonal weighting matrix in which the weights of the individual CSS are set equal to their output voltage. If, however, there are only one or two observations the system is underdetermined and the minimum norm criterion[11]

$$\hat{\boldsymbol{x}} = \boldsymbol{H}^T \left(\boldsymbol{H}\boldsymbol{H}^T\right)^{-1} \tilde{\boldsymbol{y}} \tag{10}$$

is used to determine a unique solution.

EXTENDED KALMAN FILTER (EKF) METHOD

The second estimation method is based on an extended Kalman filter approach with a state vector chosen to be the scaled sun-direction vector $\boldsymbol{d}$ in the body frame

$$\boldsymbol{x}(t) = \left[{}^{\mathcal{B}}\boldsymbol{d}(t)\right] \tag{11}$$

The reader is referred to References 11, 12, and 13 for more information on the EKF equations and their derivation. It is assumed that angular velocity measurements that follow Farrenkopf's approximation[14]

$${}^{\mathcal{G}}\tilde{\boldsymbol{\omega}}(t) = [GB]\,{}^{\mathcal{B}}\boldsymbol{\omega}(t) + {}^{\mathcal{G}}\boldsymbol{\omega}_{\beta}(t) + {}^{\mathcal{G}}\boldsymbol{\eta}_{\omega}(t) \tag{12a}$$

$${}^{\mathcal{G}}\dot{\boldsymbol{\omega}}_b(t) = {}^{\mathcal{G}}\boldsymbol{\eta}_{\omega_{\beta}}(t) \tag{12b}$$

are used for propagation where ${}^{\mathcal{B}}\boldsymbol{\omega}$ is the true body angular velocity in the body frame, ${}^{\mathcal{G}}\tilde{\boldsymbol{\omega}}$ is the measured body angular velocity in the frame of the rate gyro, $[GB]$ maps vectors written in the body frame $\mathcal{B}$ into vectors written in the gyroscope frame $\mathcal{G}$, ${}^{\mathcal{G}}\boldsymbol{\omega}_{\beta}$ is the measurement bias, and ${}^{\mathcal{G}}\boldsymbol{\eta}_{\omega}$ and ${}^{\mathcal{G}}\boldsymbol{\eta}_{\omega_{\beta}}$ are zero-mean Gaussian white-noise processes.

The scaled sun-direction vector dynamics can be written, assuming the inertial sun vector is constant, as

$$\frac{{}^{\mathcal{B}}\mathrm{d}}{\mathrm{d}t}\left[{}^{\mathcal{B}}\boldsymbol{d}(t)\right] = {}^{\mathcal{B}}\boldsymbol{d}(t) \times [BG]\left({}^{\mathcal{G}}\tilde{\boldsymbol{\omega}}(t) - {}^{\mathcal{G}}\boldsymbol{\omega}_{\beta}(t) - {}^{\mathcal{G}}\boldsymbol{\eta}_{\omega}(t)\right) - {}^{\mathcal{B}}\boldsymbol{\eta}_s(t) \tag{13}$$

where $\boldsymbol{\eta}_s$ is a zero-mean Gaussian white-noise process with $\mathrm{E}\left[\boldsymbol{\eta}_s(t)\,\boldsymbol{\eta}_s(\tau)^T\right] = \sigma_s^2\delta(t-\tau)\,\boldsymbol{I}_{3\times 3}$. Given the non-linear dynamics and measurement equations

$$\dot{\boldsymbol{x}}(t) = \boldsymbol{f}(\boldsymbol{x}(t), \boldsymbol{u}(t), \boldsymbol{\eta}(t), t), \quad \boldsymbol{\eta}(t) = \begin{bmatrix} {}^{\mathcal{B}}\boldsymbol{\eta}_s^T(t) & {}^{\mathcal{G}}\boldsymbol{\eta}_{\omega}^T(t) \end{bmatrix}^T \tag{14a}$$

$$\boldsymbol{y}_k = \boldsymbol{h}_k(\boldsymbol{x}_k, \boldsymbol{\nu}_k, t_k), \quad \boldsymbol{\nu}_k = \left[\boldsymbol{\nu}_{V,k}\right] \tag{14b}$$

the key values for the implementation of this EKF are given by

$$\boldsymbol{F}(t) \equiv \left.\frac{\partial \boldsymbol{f}}{\partial \boldsymbol{x}}\right|_{\hat{\boldsymbol{x}},\boldsymbol{u}} = \left[-\left[[BG]\,{}^{\mathcal{G}}\tilde{\boldsymbol{\omega}}(t)\right]_{\times}\right] \tag{15a}$$

$$\boldsymbol{G}(t) \equiv \left.\frac{\partial \boldsymbol{f}}{\partial \boldsymbol{\eta}}\right|_{\hat{\boldsymbol{x}},\boldsymbol{u}} = \left[-\boldsymbol{I}_{3\times 3} \quad -\left[{}^{\mathcal{B}}\hat{\boldsymbol{d}}(t)\right]_{\times}[BG]\right] \tag{15b}$$

$$\boldsymbol{H}_k \equiv \left.\frac{\partial \boldsymbol{h}_k}{\partial \boldsymbol{x}_k}\right|_{\hat{\boldsymbol{x}}_k^-} = \begin{bmatrix} H_{1,k} & \cdots & H_{N,k} \end{bmatrix}^T, \quad H_{i,k} = \begin{cases} \hat{C}_{\kappa_i}\,{}^{\mathcal{B}}\hat{\boldsymbol{n}}_i & \text{if } \frac{\hat{\boldsymbol{n}}_i^T\hat{\boldsymbol{d}}_k}{\|\hat{\boldsymbol{n}}_i\|\|\hat{\boldsymbol{d}}_k\|} \geq \cos\psi_i \\ \boldsymbol{0} & \text{if } \frac{\hat{\boldsymbol{n}}_i^T\hat{\boldsymbol{d}}_k}{\|\hat{\boldsymbol{n}}_i\|\|\hat{\boldsymbol{d}}_k\|} < \cos\psi_i \end{cases} \tag{15c}$$

$$\boldsymbol{M}_k \equiv \left.\frac{\partial \boldsymbol{h}_k}{\partial \boldsymbol{\nu}_k}\right|_{\hat{\boldsymbol{x}}_k^-} = \left\|\hat{\boldsymbol{d}}_k\right\| \mathrm{diag}\left(\hat{\boldsymbol{C}}_{\kappa}\right) \tag{15d}$$

where $[\cdot]_\times$ represents the skew-symmetric cross product matrix given by

$$\boldsymbol{a} = \begin{bmatrix} a_1 \\ a_2 \\ a_3 \end{bmatrix}, \quad [\boldsymbol{a}]_\times = \begin{bmatrix} 0 & -a_3 & a_2 \\ a_3 & 0 & -a_1 \\ -a_2 & a_1 & 0 \end{bmatrix}.$$

Note that if the current estimate of the sun direction is not within the field of view of the sensor the corresponding Kalman gain is zero. This results in strong measurements due to direct sunlight being ignored if the current estimate of the sun direction is in significant error. Because the EKF method is initialized using the WLSMN method, it is possible to have an initial guess with such error, therefore, the measurement model is modified to process any measurements above a threshold, 0.5 is used here, even if the current estimate does not predict the sensor should be receiving input.

NUMERICAL SIMULATION

A spacecraft is modeled in a 90° inclined, circular, $400\,\mathrm{km}$ altitude orbit starting on 2015 June 1, 00:00 UTC. The spacecraft is assumed to have a mass of $100\,\mathrm{kg}$, a drag area of approximately $0.38\,\mathrm{m}^2$, a ballistic coefficient of 2.1, and a cross sectional area of $1.3\,\mathrm{m}^2$ subject to SRP. Accelerations due to J_2 through J_6 Earth zonal gravitational perturbations, atmospheric drag, and solar radiation pressure (SRP) are modeled. This orbit has a period of approximately $92.5\,\mathrm{min}$ and the spacecraft spends approximately $56.6\,\mathrm{min}$ in view of the Sun per orbit. The relative positions of the Earth and Sun are simulated using ephemeris from the NASA Navigation and Ancillary Information Facility (NAIF) SPICE toolkit.[15]

The spacecraft's initial true anomaly and attitude are uniformly distributed amongst all possible values and its initial angular velocity is uniformly distributed about all three axes with a maximum value of $2.0^\circ\,\mathrm{s}^{-1}$. The spacecraft is assumed to have an inertia matrix given by $[I] = \mathrm{diag}\begin{bmatrix} 10.5 & 8.0 & 6.75 \end{bmatrix}\mathrm{kg\,m}^2$, and four reaction wheels for control purposes. In the spacecraft body frame the spin, or alignment, axes $\boldsymbol{g}_s$ for these reaction wheels are given by

$$\boldsymbol{G}_s = \begin{bmatrix} \boldsymbol{g}_{s_1} & \cdots & \boldsymbol{g}_{s_4} \end{bmatrix} = \begin{bmatrix} 0 & 0 & \cos(45^\circ) & -\cos(45^\circ) \\ \cos(45^\circ) & \sin(45^\circ) & -\sin(45^\circ) & -\sin(45^\circ) \\ \sin(45^\circ) & -\cos(45^\circ) & 0 & 0 \end{bmatrix}$$

Each reaction wheel is assumed to have a spin-axis inertia of $J_s = 0.001\,\mathrm{kgm}^2$ and a maximum torque of $30\,\mathrm{mN\,m}$. A nonlinear three-axis attitude control, as documented in Reference 16 and explained in Reference 5, is used simultaneously in conjunction with the estimators to damp out any angular velocity and orient the spacecraft toward the estimated sun direction.

The CSS alignment azimuth and elevation standard deviations are set to $\sigma_{\theta_\beta} = \sigma_{\phi_\beta} = 1.0^\circ$. All CSS are assumed to be affected by a common uniformly distributed calibration error between $0\,\%$ to $50\,\%$, and normally distributed multiplicative errors from this common value with standard deviations of $2.0\,\%$. CSS measurements are processed at $2\,\mathrm{Hz}$ and white Gaussian noise is added to each sensor with a standard deviation of 0.05.

Sensitivity to Rate Gyroscope Accuracy

Table 1 lists the values of rate gyro accuracy used in this study. These values are taken from a table of generally accepted performance grades listed in References 17 and 18. The angular acceleration white-noise process variance σ_{ω_b} is computed from the bias stability typically quoted

by gyro manufacturers as $\sigma_{\omega_b}^2 = \left(2/\tau_{\omega_r}\right)\sigma_{\omega_r}^2$, where τ_{ω_r} is the specified drift stability interval and $\boldsymbol{\omega}_r = \boldsymbol{\omega}(t_0)$.[19]

Table 1: Rate gyro accuracy levels used.

Parameter	Units	Inertial	Intermediate	Moderate	Low
Rate Noise (σ_ω)	$^\circ/\sqrt{\mathrm{s}}$	10^{-6}	10^{-4}	10^{-2}	10^{-1}
Bias Stability $\left(\sigma_{\omega_r}\right)$	$^\circ\,\mathrm{s}^{-1}$	10^{-8}	10^{-6}	10^{-3}	10^{-2}

In order to ground the values shown in Table 1, data from a smartphone equipped with an InvenSense MPU6515 MEMS gyroscope is analyzed. According to the manufacturer specifications[20] the gyro is expected to have a rate noise spectral density of $0.01\,^\circ/\sqrt{\mathrm{s}}$. The calculated noise statistics for the actual gyro are shown in Table 2. As can be seen the measurement rate noise spectral density is within the manufacturer specification and the noise statistics place this gyro between the intermediate and moderate performance grades listed in Table 1.

Table 2: Calculated rate gyro noise statistics for InvenSense MPU6515 gyroscope.

Axis	σ_ω, $^\circ/\sqrt{\mathrm{s}}$	σ_{ω_r}, $^\circ/\mathrm{s}^{3/2}$	σ_{ω_β}, $^\circ\,\mathrm{s}^{-1}$
X	0.0051	0.0034	0.00068
Y	0.0059	0.0035	0.00062
Z	0.0052	0.0025	0.00076
Average	0.0054	0.0031	0.00068

The results of a 1000 case Monte Carlo analysis in which the level of gyroscope accuracy is varied are shown in Figure 2. The calculated 3σ error bounds of the total angular error in the estimate of the scaled sun-direction vector are shown Figure 2a and the total time that the spacecraft spent with an estimation error in excess of 10° is shown in Figure 2b. It should be noted that the WLSMN method does not use the gyroscope measurements for propagation. Because the rates are only used by the control to damp out any rotational motion there is no significant difference in the WLSMN method when altering the gyro performance, therefore, only the results of the intermediate level gyro accuracy are shown.

As can be seen, the EKF method generates nearly identical results using the inertial and intermediate grade rate gyro performance levels. The performance of the simultaneous estimation and control of the EKF method only noticeably suffers when the rate gyro is reduced to low level accuracy. Even when reduced to levels lower than available in mass market commercial MEMS gyroscopes, the EKF method outperforms the WLSMN method. However, the WLSMN is still able to achieve sun pointing from an unknown tumble in time to spend the majority of its orbit pointed to within a stringent 10° threshold.

The total calculation time of the propagation and measurement updates are computed for both methods over the entire $100\,\mathrm{min}$ simulation. The average and standard deviations of the computation times, for C code compiled on a Windows i7 $2.5\,\mathrm{GHz}$ machine, are shown in Table 3. The EKF propagation update is computed using an RK4 integrator. While this is not flight hardware, the relative difference shows there is very little difference in estimation time, but the WLSMN method

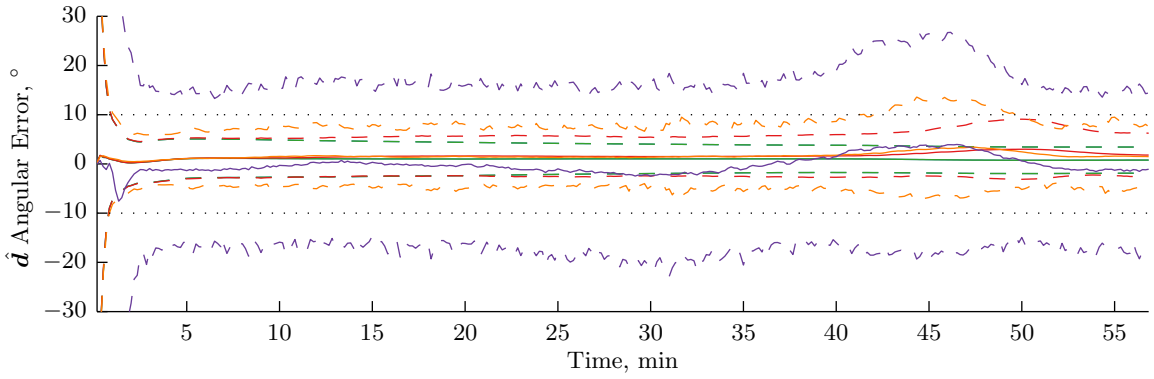

(a) Sun-direction estimate total angular error, mean (solid) and 3σ (dashed).

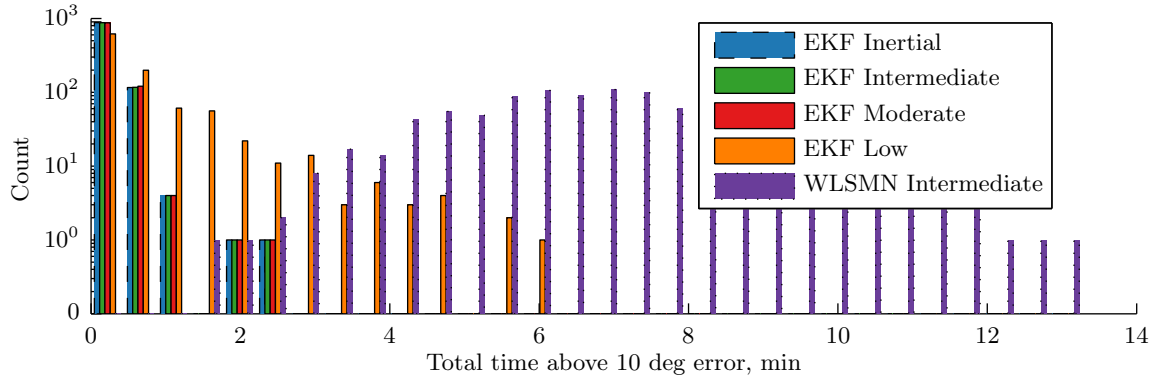

(b) Total time spent with estimate in error of more than 10°.

Figure 2: 1000 case Monte Carlo analysis results for varying levels of gyro accuracy.

Table 3: Averages and standard deviations for computation times of various filters.

Method	Propagation Update, µs	Measurement Update, µs
EKF	1.74 ± 0.57	1.28 ± 1.09
WLSMN	-	1.21 ± 0.52

benefits from a lack of propagation.

Sensitivity to Sensor Failure

When using an underdetermined configuration, as shown in Figure 1, sensor failure is a key concern. Figure 3 shows a coverage map for when CSS 1 fails. As can be seen, a single sensor failure results in a significant area with zero sensor coverage and reduced coverage by three or more sensors. While the single-point estimation scheme will obviously fail when the Sun is this region of zero coverage, the EKF based approach is capable of propagating through such a dead zone given sufficient prior measurements. It is possible that, because regulation control is being performed simultaneous to sun-direction estimation, the spacecraft's angular velocity can be brought to zero with the spacecraft in an attitude where the Sun is only visible to a failed sensor. This is easily

avoided by delaying all control efforts when no sensors are reporting measurements above some threshold, 0.5 is used here. The cases that use this additional control delaying logic are labeled as "Delayed Ctrl" in the Monte Caro analysis plots.

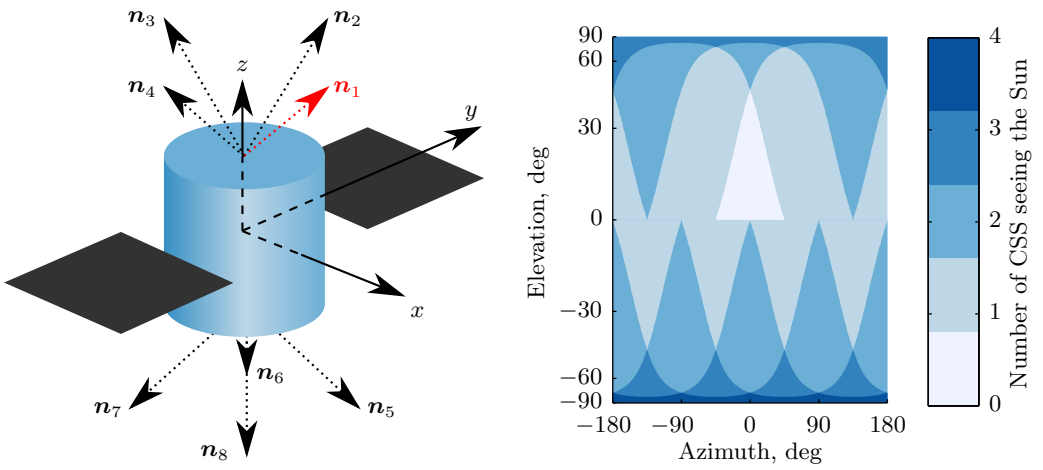

(a) Schematic of spacecraft, $\theta = 45°$.

(b) CSS coverage map.

Figure 3: Illustration of spacecraft with CSS unit vectors $\boldsymbol{n}_i$ for a dual pyramid configuration with a single sensor failure and the associated CSS coverage map shown on a cylindrical projection.

The results of a 1000 case Monte Carlo analysis run simulating a known failure of CSS 1 are shown in Figures 4 to 6. The calculated 3σ error bounds of the total angular error in the estimate of the scaled sun-direction vector are shown along with the total time that the spacecraft spent with an estimation error in excess of $10°$. Results for the EKF method are shown for the intermediate and low gyro levels, and the WLSMN estimator results are shown for intermediate level gyro performance. The nominal full sensor suite performances are reproduced from Figure 2 for comparison.

The WLSMN estimation method suffers significantly with a single sensor failure as compared to the nominal performance. Even though all cases are able to point in the general direction of the Sun, many fail to stably maintain pointing accuracy and spend the majority of the orbit pointed greater than $10°$ away from the Sun. Unfortunately, delaying the control when no CSS are reporting measurements does little to improve the sun-pointing performance.

The EKF method shows better results. The majority of the intermediate level gyro cases spend fewer than $6\,\text{min}$ outside the $10°$ threshold. However, several cases never achieve sun-pointing. In these cases, the control halts all angular motion and the spacecraft comes to rest in an attitude with the Sun only in view of the failed sensor. Applying the delayed control logic helps avoid this with only two cases spending longer than $6\,\text{min}$ with an error greater than $10°$. Similar trends are seen when using the EKF method with low level rate gyros. The performance is degraded compared to the nominal full sensor suite, but all cases quickly converge and spend the majority fo the orbit pointed within $10°$ of the Sun.

CONCLUSION

This paper examines the sensitivity of two sun-direction estimation schemes, both using underdetermined sensor configurations, to rate gyroscope noise and known CSS sensor failure. Both

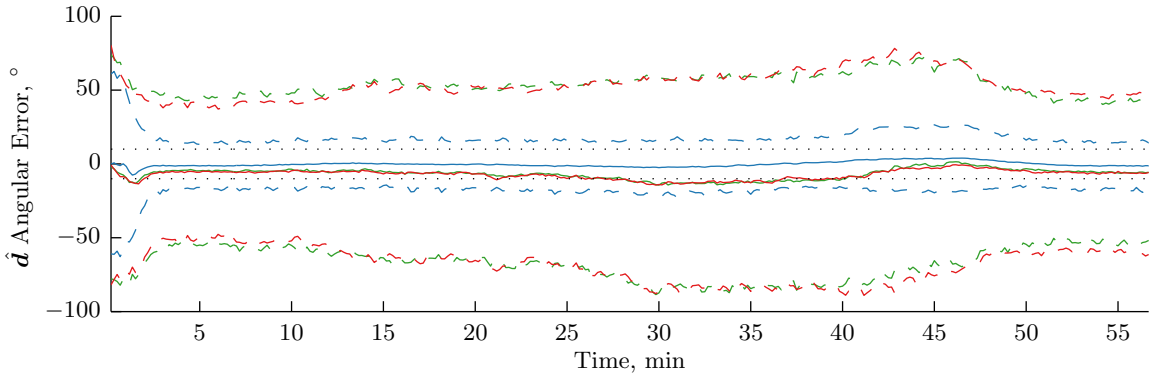

(a) Sun-direction estimate total angular error, mean (solid) and 3σ (dashed).

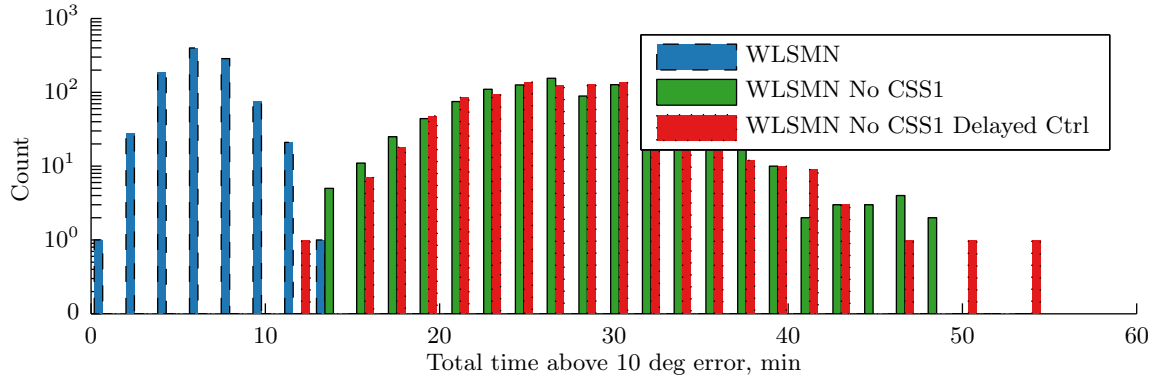

(b) Total time spent with estimate in error of more than 10°.

Figure 4: 1000 case Monte Carlo analysis results for WLSMN method with known single CSS failure and intermediate gyro performance.

estimation techniques, one a single-point estimator and one a sequential estimator, provide an estimate of the sun-direction vector in the body frame without any knowledge of a spacecraft's inertial position despite significant noise and without modeling the input due to Earth's albedo. Numerical simulations shown that sun pointing, to less than 10° accuracy, is quickly achieved by both methods even using rate gyroscope with performance lower than that available in mass market commercial electronics MEMS gyroscopes. Note that this results is achieved despite simulating sensor input biases due to Earth's albedo and sensor alignment corruptions. The weighted least squares minimum norm method has half the computation cost of the extended Kalman filter approach. However, the performance of the WLSMN method degrades more severely in the face of known sensor failure. The EKF method is shown to lose a little accuracy if the sensor failure is known, but still quickly converges to a sun-pointed attitude. Future work will investigate methods to autonomously detect sensor failure in order to take advantage of this lack of performance degradation immediately post launch vehicle separation if a sensor were to fail.

REFERENCES

[1] P. Appel, "Attitude Estimation from Magnetometer and Earth-Albedo-Corrected Coarse Sun Sensor Measurements," *Acta Astronautica*, Vol. 56, Jan. 2005, pp. 2–5, 10.1016/j.actaastro.2004.09.001.

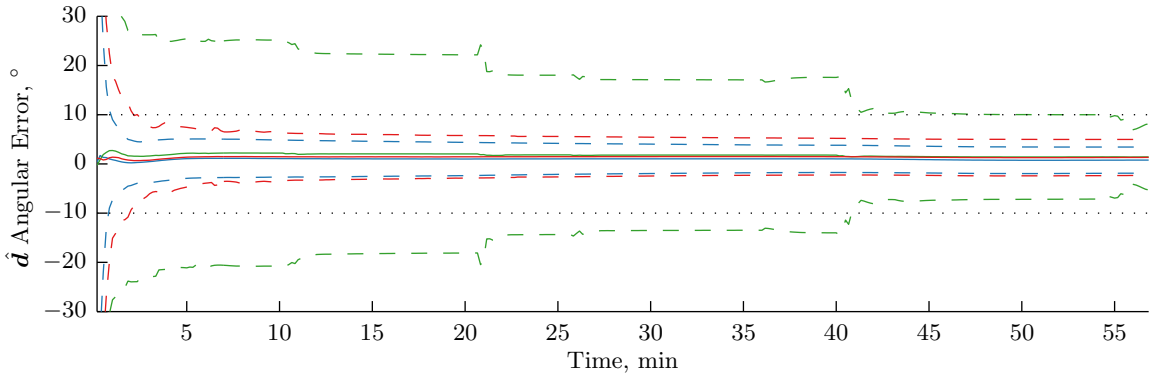

(a) Sun-direction estimate total angular error, mean (solid) and 3σ (dashed).

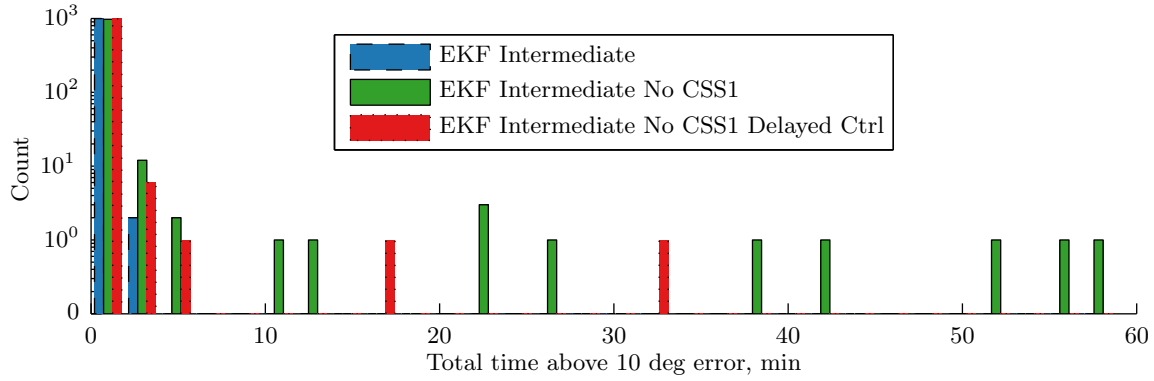

(b) Total time spent with estimate in error of more than 10°.

Figure 5: 1000 case Monte Carlo analysis results for EKF method, using intermediate level rate gyros, with known single CSS failure.

[2] H. Jung and M. L. Psiaki, "Tests of Magnetometer/Sun-Sensor Orbit Determination Using Flight Data," *Proceedings of the AIAA Guidance, Navigation, and Control Conference and Exhibit*, No. August, Montreal, Canada, American Institute of Aeronautics and Astronautics, Aug. 2001.

[3] G. Rufino, M. Grassi, and M. Rolfi, "Preliminary Calibration Results For a High-Precision CMOS Sun Sensor," *Proceedings of the AIAA Guidance, Navigation, and Control Conference and Exhibit*, No. August 2008, Honolulu, HI, Aug. 2011, pp. 1–9.

[4] K. Ninomiya, Y. Ogawara, K. Tsuno, and S. Akabane, "High Accuracy Sun Sensor Using CCDs," *Proceedings of the AIAA Guidance, Navigation, and Control Conference*, Minneapolis, MN, American Institute of Aeronautics and Astronautics, 1988.

[5] S. A. O'Keefe and H. Schaub, "Sun Heading Estimation Using Underdetermined Set of Coarse Sun Sensors," *Proceedings of the AAS/AIAA Astrodynamics Specialist Conference*, Hilton Head, SC, Aug. 2013.

[6] B. Jackson and B. Carpenter, "Optimal Placement of Spacecraft Sun Sensors Using Stochastic Optimization," *Proceedings of the IEEE Aerospace Conference*, Big Sky, MT, IEEE, Mar. 2004, pp. 3916–3923.

[7] J. C. Springmann and J. W. Cutler, "Optimization of Directional Sensor Orientation with Application to Photodiodes for Spacecraft Attitude Determination," *Proceedings of the AAS/AIAA Space Flight Mechanics Conference*, Kauau, HI, Feb. 2013, pp. 1–19.

[8] G. M. Lerner, *Spacecraft Attitude Determination and Control*, ch. Sun Sensors, pp. 155–166. Dordrecht, The Netherlands: D. Reidel Publishing Co., 1978.

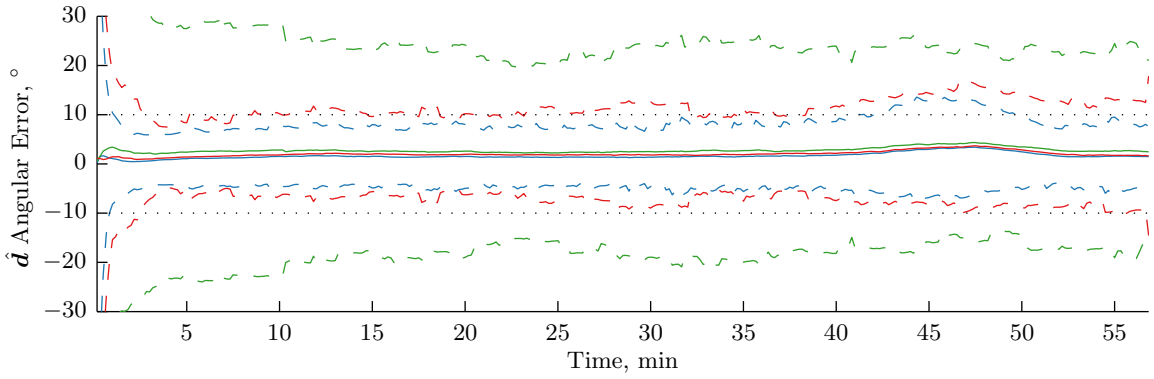

(a) Sun-direction estimate total angular error, mean (solid) and 3σ (dashed).

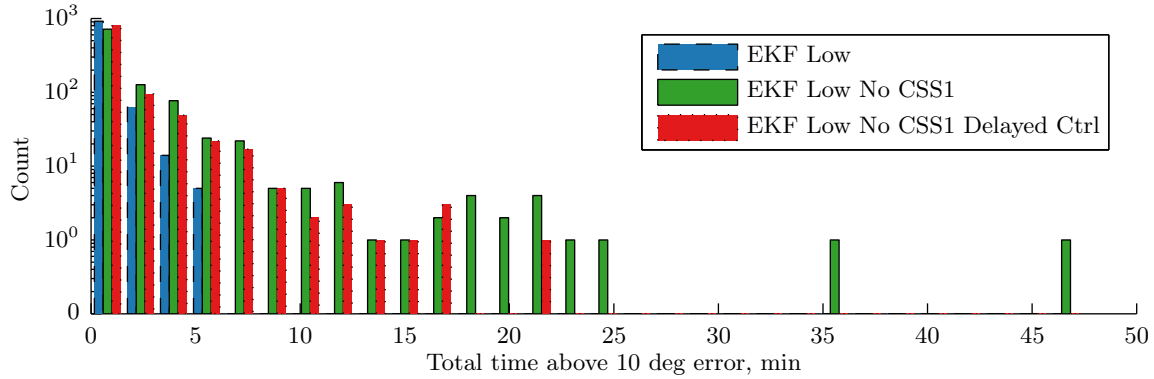

(b) Total time spent with estimate in error of more than 10°.

Figure 6: 1000 case Monte Carlo analysis results for EKF method, using low level rate gyros, with known single CSS failure.

[9] D. D. V. Bhanderi and T. Bak, "Modeling Earth Albedo for Satellites in Earth Orbit," *Proceedings of the AIAA Guidance, Navigation, and Control Conference and Exhibit*, San Francisco, CA, American Institute of Aeronautics and Astronautics, Aug. 2005.

[10] J. P. Snyder, *Map Projections: A Working Manual*, pp. 76–85. Geological Survey (U.S.) Professional Paper 1395, 1987.

[11] B. Tapley, B. Schutz, and G. Born, *Statistical Orbit Determination*. Elsevier Academic Press, 2004.

[12] J. L. Crassidis and J. L. Junkins, *Optimal Estimation of Dynamic Systems*. Boca Raton, FL: Chapman and Hall/CRC Press, 2004.

[13] D. Simon, *Optimal State Estimation*. John Wiley & Sons, Inc., 2006.

[14] R. L. Farrenkopf, "Analytic Steady-State Accuracy Solutions for Two Common Spacecraft Attitude Estimators," *Journal of Guidance, Control, and Dynamics*, Vol. 1, No. 4, 1978, pp. 282–284, 10.2514/3.55779.

[15] C. Acton, "Ancillary Data Services of NASA's Navigation and Ancillary Information Facility," *Planetary and Space Science*, Vol. 44, No. 1, 1996, pp. 65–70.

[16] E. A. Hogan and H. Schaub, "Three-Axis Attitude Control using Redundant Reaction Wheels with Continuous Momentum Dumping," *Proceedings of the AAS/AIAA Spaceflight Mechanics Conference*, Kauai, HI, American Institute of Aeronautics and Astronautics, Feb. 2013.

[17] M. S. Grewal, L. R. Weill, and A. P. Andrews, *Global Positioning Systems, Inertial Navigation, and Integration*, ch. 6, pp. 131–178. John Wiley & Sons, Inc., 2001.

[18] M. Grewal and A. Andrews, "How Good Is Your Gyro? [Ask the Experts]," *IEEE Control Systems Magazine*, Vol. 30, Feb. 2010, pp. 12–86, 10.1109/MCS.2009.935122.

[19] M. E. Pittelkau, "Everything is Relative in Spacecraft System Alignment Calibration," *Journal of Spacecraft and Rockets*, Vol. 39, No. 3, 2002, pp. 460–466, 10.2514/2.3830.

[20] InvenSense, "MPU-6500 Product Specification," tech. rep., InvenSense, San Jose, CA, 2014.